foods

MDPI

Article

The Mechanism of *Grifola frondosa* Polysaccharides in Alleviating Radiation-Induced Damage via Improvement of Antioxidant Activity and Regulation of Immunity as Well as Gut Microbiota

Xianguo Zou [1], Shumin Zou [1], Mingjie Shen [1], Guohua Ji [2], Peilong Sun [1], Hangjun Chen [3], Guofu Feng [4] and Kai Yang [1,*]

[1] College of Food Science and Technology, Zhejiang University of Technology, Hangzhou 310014, China; xianguozou2019@zjut.edu.cn (X.Z.); 221124260063@zjut.edu.cn (S.Z.); mingjie_shen1998@163.com (M.S.); sun_pl@zjut.edu.cn (P.S.)
[2] Hangzhou Huaxian High-Tech Co., Ltd., Hangzhou 310020, China; jiguohua10@126.com
[3] Food Science Institute, Zhejiang Academy of Agricultural Sciences, Hangzhou 325005, China; spshangjun@sina.com
[4] Zhejiang Jolly Pharmaceutical Co., Ltd., Huzhou 313200, China; fgfok@21cn.com
* Correspondence: yangkai@zjut.edu.cn

Abstract

Grifola frondosa polysaccharides (GFPs) have garnered increasing interest for their diverse bioactivities, yet their radioprotective potential remains underexplored. The crude polysaccharide fraction (GFP60), obtained via graded ethanol precipitation and hot water extraction, was identified as the most promising fraction to protect radiation-induced damage in BALB/c mice. GFP60 attenuated radiation-induced weight loss, and mitigated splenic, thymic and hepatic tissues. Biochemically, GFP60 dose-dependently alleviated damage to white blood cells, red blood cells, and platelets and reduced bone marrow DNA damage. In addition, GFP60 lowered serum malondialdehyde (MDA) and restored superoxide dismutase (SOD) and glutathione peroxidase (GSH-Px) activities, indicating enhanced redox homeostasis. Immunologically, it restored serum immunoglobulins (IgA, IgM, and IgG). Moreover, GFP60 modulated gut microbial diversity, as reflected by increased ASVs and Chao1 index, reduced *Bacteroides* abundance and promoted *Lachnospiraceae_NK4A136_group*. PCoA and UPGMA clustering further confirmed that GFP60 treatment shifted the gut microbiota profile toward that of normal controls, with LEfSe analysis indicating reduced compositional divergence in medium- and high-dose groups. Collectively, these findings suggest that GFP60 may attenuate radiation-induced injury, potentially through coordinated modulation of oxidative stress, immune function, and gut microbiota, supporting its potential as a promising natural radioprotective agent.

Keywords: *Grifola frondosa*; fractionated polysaccharides; radioprotection; oxidative stress; gut microbiota

Check for updates

Academic Editor: Aldona Sobota

Received: 1 October 2026
Revised: 12 November 2026
Accepted: 16 November 2026
Published: 18 November 2026

Copyright: © 2026 by the authors. Licensee MDPI, Basel, Switzerland. This article is an open access article distributed under the terms and conditions of the Creative Commons Attribution (CC BY) license.

1. Introduction

Radiation is ubiquitous in the environment. It can generate free radicals via ionization and induce DNA strand breaks, preferentially targeting rapidly dividing cells. Prolonged exposure to harmful levels of radiation causes substantial damage to multiple organ systems, particularly the hematopoietic, immune, gastrointestinal systems [1]. In the hematopoietic

system, radiation directly damages hematopoietic stem cells and alters the ability of bone marrow stromal components to support and/or maintain hematopoiesis both in vivo and in vitro [2]. In the immune system, the effects of radiation are highly dose-dependent: high-dose radiation directly damages immune cells and causes immune dysfunction [3], whereas the effects of low-dose radiation are influenced by multiple factors, including genetic background, radiation type, dose, and individual variability, resulting in complex immunomodulatory effects and potentially biphasic responses [4,5]. In the gastrointestinal system, radiation-induced injury is characterized by intestinal stem cell depletion, impaired epithelial regeneration, barrier disruption, and subsequent bacterial translocation leading to sepsis; clinically, this manifests as nausea, vomiting, diarrhea, and other gastrointestinal symptoms [6,7]. Moreover, studies have demonstrated that radiation exposure shortens lifespan, increases the incidence of chronic diseases, and accelerates aging [8,9].

Common radioprotective agents include aminothiols, cytokines, antioxidants, and natural products. Natural products, as sources of radioprotective agents, offer numerous advantages, such as low toxicity and cost-effectiveness [10]. Natural polysaccharides from *Aloe vera*, *Angelica sinensis*, and *Astragalus membranaceus* have been proven to provide radioprotective effects [11]; however, the precise mechanisms underlying its radioprotective effects and its relationship with the gut microbiota remain unclear.

Grifola frondosa serve as a typical representative of medicinal and edible fungi, renowned in China for their nutritional and pharmacological properties, containing various bioactive components such as polysaccharides, polypeptides, polyphenols, and sterols. They have a long history of safe consumption and represent commercially significant fungi [12]. *Grifola frondosa* polysaccharides (GFPs), the primary active components in *Grifola frondosa*, possess various biological activities, including antioxidant [13], antitumor [14], immunomodulatory [15] and hypoglycemic and hypolipidemic activities [16]. Notably, demonstrating its established safety and clinical value, GFP was approved in China in 2010 as an adjunctive therapeutic drug for cancer treatment [17]. Furthermore, driven by its multiple health benefits, *Grifola frondosa* polysaccharide combined with polymerized whey protein has been utilized as a functional additive to improve the quality of yogurt [18]. It remains unclear whether GFPs possess radioprotective properties, and the mechanisms by which they might exert such effects have not yet been elucidated.

In this study, three crude polysaccharide fractions (GFP40, GFP60, and GFP80) were sequentially extracted and fractionated from *Grifola frondosa*, among which GFP60 was selected for its optimal efficacy. We selected highly radiosensitive BALB/c mice as the in vivo model, investigated GFP60's protective effects and underlying mechanisms against acute radiation-induced injury in mice, and found that it exerted effective radioprotective activity through multiple mechanisms, including reducing serum oxidative stress markers, protecting DNA integrity, enhancing humoral immunity, and remodeling gut microbial diversity. This study provides experimental evidence and novel insights for the development of GFP60 as a potential natural radioprotective agent.

2. Materials and Methods

2.1. Materials

Fruiting bodies of *Grifola frondosa* were supplied by Zhejiang Huihe Health Technology Co., Ltd. (Lishui, China). Six-week-old male SPF-grade BALB/c mice (body weight: 20 ± 2 g) were purchased from the Laboratory Animal Center of Hangzhou Medical College (Hangzhou, China). The following reagents were obtained from Sinopharm Chemical Reagent Co., Ltd. (Shanghai, China): ethanol, glucose, potassium persulfate ($K_2S_2O_8$, GR), perchloric acid (GR), calcium chloride, PBS buffer, and 2,2′-azino-bis (3-ethylbenzothiazoline-6-sulfonic acid) (ABTS). 2,2-diphenyl-1-picrylhydrazyl (DPPH)

was purchased from Beijing Solarbio Science & Technology Co., Ltd. (Beijing, China). Bovine serum albumin (BSA, BR) was provided by Shanghai Yuanye Bio-Technology Co., Ltd. (Shanghai, China). Potassium ferricyanide, trichloroacetic acid, and ferric chloride were purchased from Shanghai Macklin Biochemical Technology Co., Ltd. (Shanghai, China). Amifostine and fetal bovine serum (FBS) were supplied by Dalian Meilun Biotechnology Co., Ltd. (Dalian, China). Paraformaldehyde was obtained from Aladdin Biochemical Technology Co., Ltd. (Shanghai, China). The superoxide dismutase (SOD), glutathione peroxidase (GSH-Px), and malondialdehyde (MDA) assay kits and cell counting kit-8 (CCK-8) were purchased from Nanjing Jiancheng Bioengineering Institute (Nanjing, China). The immunoglobulin M (IgM), immunoglobulin A (IgA), and immunoglobulin G (IgG) enzyme-linked immunosorbent assay (ELISA) kits were purchased from Jingmei Bioengineering Co., Ltd. (Shenzhen, China). All chemicals were of analytical grade unless otherwise specified.

2.2. Preparation of Fractionated GFP

The extraction process followed previously reported methods with adjustments [19,20]. The *Grifola frondosa* was dried in an oven at 60 °C for 8 h until a constant weight was achieved and then ground into powder and sieved through 40-mesh screen. The powder was defatted with 95% ethanol at room temperature for 24 h, followed by centrifugation to remove the ethanol, and then air-dried for later use. The above powder of 200 g was mixed with deionized water at a solid-to-liquid ratio of 1:25 (w/v) and subjected to hot water extraction at 80 °C for 4 h. The mixture was centrifuged, and the supernatant was concentrated by rotary evaporation at 60 °C and 100 r/min to obtain the *Grifola frondosa* aqueous extract. The aqueous extract was dissolved in a small volume of water and deproteinized using the Sevag method [21]. The polysaccharide solution was mixed with Sevag reagent at a volume ratio of 3:1, where the Sevag reagent consisted of chloroform and n-butanol at a volume ratio of 4:1. The mixture was placed in a separatory funnel, vigorously shaken for 15 min, and allowed to stand for 30 min for phase separation. The protein layer and the organic solvent layer were then discarded. This procedure was repeated until no protein layer remained. Finally, residual chloroform was removed by rotary evaporation under reduced pressure at 60 °C and 0.09 MPa. An appropriate amount of anhydrous ethanol was slowly added to the rotary-evaporated aqueous extract under stirring until the final ethanol concentration in the system reached 40%. Followed by precipitation at room temperature overnight, the solution was centrifuged at 8000 r/min for 20 min, and the precipitate was collected, redissolved in water, and subjected to rotary evaporation to remove excess ethanol. The concentrate was then freeze-dried and named GFP40. To the supernatant obtained after the removal of the precipitate, anhydrous ethanol was further added under continuous stirring until the final ethanol concentration reached 60%. The above procedure was repeated to obtain the crude *Grifola frondosa* polysaccharide, designated as GFP60. Subsequently, to the remaining supernatant, anhydrous ethanol was added once again under stirring to reach a final concentration of 80%. Following the same procedure, the crude polysaccharide was obtained and named GFP80. The three fractions, GFP40, GFP60, and GFP80, were then collected and stored in a desiccator for later use.

2.3. Determination of the Principal Components of Fractionated GFP

The total carbohydrate content of GFP samples were determined using the phenol-sulfuric acid method [22]. Briefly, GFP40, GFP60 or GFP80 was dissolved in sterilized distilled water (0.1 mg/mL), and 1 mL of this solution was mixed with 1 mL of 5% phenol and 5 mL of concentrated sulfuric acid. The mixture was incubated in the dark at 25 °C for 30 min, and the absorbance was measured at 490 nm. A glucose standard curve

was constructed using the same procedure, and the total carbohydrate content was calculated accordingly.

BSA standards and GFP samples were added to a microplate. Then, BCA working reagent was added, mixed for 30 s, and incubated at 37 °C for 30 min. Absorbance was measured at 562 nm, and protein concentrations in GFP samples were calculated using the BSA standard curve [23].

2.4. Determination of Free Radical Scavenging Capacity and Cytoprotective Activities of Fractionated GFP

2.4.1. ABTS Radical Scavenging Activity

Referring to the experimental method [24] with slight modifications, 0.20 mL of 7.40 mM ABTS was mixed with 0.20 mL of 2.60 mM $K_2S_2O_8$ and allowed to react at room temperature in the dark for 12 h. The mixture was then diluted 25–50 times with 95% ethanol until A734 = 0.70 ± 0.02 to obtain the $ABTS^+$ working solution. Different stock concentrations of the test samples (GFP40, GFP60 and GFP80) were diluted to 0, 0.05, 0.10, 0.20, 0.50, and 1.00 mg/mL with distilled water. Then, 0.80 mL of the $ABTS^+$ working solution was mixed with 0.20 mL of the test sample, thoroughly mixed, and left to stand for 6 min. The absorbance was measured at 734 nm. A blank control was measured by replacing the ABTS solution with 95% ethanol to determine the background absorbance of the sample. Each measurement was performed in triplicate.

$$ABTS \text{ radical scavenging rate } (\%) = \frac{A0 - Ai + Aj}{A0} \times 100 \quad (1)$$

where A0 is absorbance of the $ABTS^+$ working solution mixed with 95% ethanol, Ai is absorbance of the $ABTS^+$ working solution mixed with the sample and Aj is absorbance of the sample mixed with 95% ethanol.

2.4.2. DPPH Radical Scavenging Activity

Following the experimental method in [25] with slight modifications, test solutions (GFP40, GFP60 and GFP80) were prepared at stock concentrations of 0, 0.10, 0.20, 0.50, 1.00 and 2.00 mg/mL with distilled water. Then, 2.00 mL of each test solution was added to a test tube, followed by an equal volume of freshly prepared 0.2 mmol/L DPPH in 95% ethanol. The mixture was vortexed and incubated in the dark at 37 °C for 30 min, and the absorbance was measured at 517 nm. The background absorbance of the samples was determined using 95% ethanol as a blank. All experiments were performed in triplicate.

$$DPPH \text{ radical scavenging rate } (\%) = \frac{A0 - Ai + Aj}{A0} \times 100 \quad (2)$$

where A0 is absorbance of the DPPH working solution mixed with 95% ethanol, Ai is absorbance of the DPPH working solution mixed with the sample and Aj is absorbance of the sample mixed with 95% ethanol.

2.4.3. Total Reducing Power Assay

Following the previously described method [26], test solutions (GFP40, GFP60 and GFP80) were prepared at stock concentrations of 0, 0.30, 0.90, 1.80, 3.60, and 7.20 mg/mL with distilled water. Then, 0.2 mL of each sample solution was mixed with 0.50 mL of distilled water and 0.50 mL of 1% (w/v) potassium ferricyanide solution. The mixture was incubated in a 50 °C water bath for 20 min. After the reaction, 0.5 mL of 10% (w/v) trichloroacetic acid solution was added to terminate the reaction. Subsequently, the mixture was centrifuged, and 0.5 mL of the supernatant was collected and mixed with an equal volume of distilled water and 0.1 mL of 0.1% (w/v) ferric chloride solution. After standing

at room temperature for 10 min, the absorbance was measured at 700 nm. All experiments were performed in triplicate.

2.4.4. Assessment of the Radioprotective Effect of Fractionated GFP on Cells

RAW 264.7 cells were seeded in 96-well plates at a density of 5×10^4 cells per well. After 24 h of incubation, the complete medium was removed and replaced with fresh medium containing different concentrations (100, 200, and 400 μg/mL) of GFP40, GFP60, or GFP80 (all polysaccharides were dissolved in complete medium supplemented with 10% fetal bovine serum) based on previously reported non-cytotoxic concentration ranges [27]. Following another 24 h incubation period, the cells were subjected to ^{60}Co-γ radiation at a total raiation dose of 8 Gy according to the described method [28]. After irradiation, the original medium was replaced with an equal volume of fresh complete medium, and the cells were further incubated for 24 h. Cell viability was then assessed using the cell counting kit-8 (CCK-8) assay kit (Nanjing Jiancheng Bioengineering Institute, Nanjing, China).

2.5. Animal Experiments

2.5.1. Animal Housing and Maintenance

Six-week-old male SPF-level BALB/c mice, obtained from Zhejiang Center of Laboratory Animals, were housed in the Laboratory Animal Center of Zhejiang Academy of Agricultural Sciences in a specific pathogen-free (SPF) barrier environment maintained at a constant temperature of 22 ± 2 °C, at a relative humidity of 60 ± 5%, and under a 12 h light/dark cycle. The mice were provided with a standard rodent diet (AIN-93) and sterile water ad libitum. To ensure experimental rigor and reliability of the results, all cages were thoroughly washed and sterilized, and drinking water bottles along with the water itself were autoclaved prior to the experiment. All procedures strictly adhered to the guidelines for the use of SPF-level animals. All animal procedures were approved by the Institutional Animal Care and Use Committee of Zhejiang Academy of Agricultural Sciences (Approval No. 25ZALAS44) and were conducted in accordance with the relevant guidelines and regulations for the care and use of laboratory animals.

2.5.2. Establishment of Radiation Injury Model and Experimental Grouping

After 7 days of acclimatization, a total of forty-eight mice were randomly divided into six groups ($n = 8$ per group) using a body weight-based stratified randomization method to ensure the initial weight variation among groups did not exceed 1 g. The six groups were designated as follows: normal control (NC), model control (MC), positive control (PC), GFP60 low-dose (GFPL), GFP60 medium-dose (GFPM), and GFP60 high-dose (GFPH) groups. Mice in the GFPL, GFPM, and GFPH groups were administered GFP60 intragastrically (i.g.) at doses of 100, 200, and 400 mg/kg, respectively, daily for 21 consecutive days. The NC, MC, and PC groups received an equal volume of sterile saline by the same route over the same period. On day 22, all mice except those in the NC group were subjected to a single whole-body irradiation with ^{60}Co-γ rays at a total dose of 5 Gy [29]. The PC group received a single intraperitoneal injection of amifostine (150 mg/kg, 0.3 mL per mouse) 1 h prior to irradiation. Body weight was recorded and fecal samples were collected from the all mice on day 24. After a 12 h interval, the all mice were fasted with free access to water, and were euthanized on day 25 for blood collection via the retro-orbital plexus.

2.5.3. Sample Collection

Half of each blood sample was immediately transferred into ethylenediaminetetraacetic acid (EDTA)-coated Eppendorf (EP) tubes for complete blood count analysis. The remaining half was allowed to clot at 4 °C for 4 h and then centrifuged to isolate serum, which was stored at −80 °C.

After euthanasia, the liver, thymus, spleen, colon, and both femurs were collected. The thymus, and spleen were rinsed, blotted dry, and weighed. Portions of the spleen and ileum were fixed in 4% paraformaldehyde for H&E staining and histological sectioning. The remaining tissues were flash-frozen in liquid nitrogen and stored at −80 °C.

2.6. Measurement of Mouse Body Weight

Body weight measurements were taken at three time points: before the initial gavage on day 1, pre-irradiation, and pre-dissection.

2.7. Determination of Organ Index

During dissection, the liver, thymus, and spleen were collected and weighed. The organ indices were calculated as follows:

$$\text{Thymic index (\%)} = \text{Thymus weight (g)/Body weight (g)} \times 100$$

$$\text{Spleen index (\%)} = \text{Spleen weight (g)/Body weight (g)} \times 100$$

$$\text{Liver index (\%)} = \text{Liver weight (g)/Body weight (g)} \times 100$$

2.8. Determination of Peripheral Blood Parameters in Mice

Blood was collected from the retro-orbital plexus of the mice. The whole blood was immediately transferred into EDTA-anticoagulated EP tubes. The numbers of peripheral white blood cells (WBCs), red blood cells (RBCs), and platelets (PLTs) in all groups were analyzed using an automated hematology analyzer (Shenzhen Mindray Bio-Medical Electronics Co., Ltd., Shenzhen, China).

2.9. Assessment of Bone Marrow DNA Damage

The determination of DNA damage in bone marrow was performed according to the previously described method with slight modifications [30]. The left femur was isolated from the mouse and dissected free of surrounding muscle tissue. Both ends of the bone were cut open, and the bone marrow was flushed into a centrifuge tube using 10 mL of a 0.005 mol/L $CaCl_2$ solution. After repeated flushing, the suspension was left to stand at 4 °C for 30 min. Subsequently, it was centrifuged at 2500 rpm for 15 min. The pellet was collected and subjected to acidification with 5 mL of 0.2 mol/L $HCLO_4$. After thorough mixing, the mixture was incubated in a 90 °C water bath for 15 min. Following cooling under running water, the sample was centrifuged again at 2500 rpm for 15 min. The resulting supernatant was collected, and its absorbance was measured at 260 nm using an ultraviolet–visible spectrophotometer (Thermo Fisher Scientific, Waltham, MA, USA) to quantify the DNA content in the bone marrow. The DNA content (μg) was calculated according to the following formula: DNA (μg) = $40 \times 50 \times A_{268}$.

2.10. Determination of Serum Levels of SOD, MDA, and GSH-Px in Mice

Serum levels of MDA, SOD, and GSH-Px were measured in all groups of mice using commercial assay kits following the manufacturer's protocols.

2.11. Measurement of Immunoglobulin Levels

Measurement of serum immunoglobulin A (IgA), immunoglobulin M (IgM), and immunoglobulin G (IgG) levels in all mouse groups was conducted using commercial ELISA kits according to the supplied instructions.

2.12. Histomorphological Observation

Following euthanasia, the collected colon and spleen tissues were fixed in 4% paraformaldehyde, dehydrated through a graded ethanol series, embedded in paraffin, and sectioned at a thickness of 4 μm. Subsequently, the sections were stained with hematoxylin and eosin (H&E) for histological examination.

2.13. Gut Microbiota Analysis

Microbial Genomic DNA was extracted from mouse fecal pellets. The V3-V4 hypervariable region of the bacterial 16S rRNA gene was amplified by polymerase chain reaction (PCR) using the custom barcoded primers 341F (5′-CCTACGGGNGGCWGCAG-3′) and 806R (5′-GGACTACHVGGGTWTCTAAT-3′). Paired-end reads were merged using fast length adjustment of short reads (FLASH) software (version 1.2.11) to generate clean Tags. Subsequent data analysis was performed as follows: Alpha diversity indices, including rarefaction curves, Shannon curves, and rank-abundance curves, were calculated using Mothur software (version 1.48.1). Both Alpha and Beta diversity analyses were conducted with quantitative insights into microbial ecology (QIIME) software (version 2024.10). Principal Component Analysis (PCA) and Multi-Dimensional Scaling (MDS) based on the Binary Jaccard distance were performed using the R (version R 4.4.1) language environment. Operational taxonomic units (OTUs) were classified taxonomically by alignment against reference databases. Finally, microbial community composition and relative abundance were analyzed and visualized using QIIME software.

2.14. Data Analysis

All statistical analyses were performed using SPSS version 19.0. Prior to analysis, the assumptions of normality and homogeneity of variance were tested. For data meeting the assumptions of normality and homogeneity of variance, a one-way analysis of variance (ANOVA) followed by Tukey's post hoc test was used for multiple comparisons. For data that did not meet the assumption of homogeneity of variance, Welch's ANOVA followed by Tamhane's T2 post hoc test was applied. For the gut microbiota data, a one-way analysis of variance (ANOVA) was applied. To evaluate the differences in microbial indices among the treatment groups, Dunnett's post hoc test was applied, comparing all groups against the MC group. Differences were considered statistically significant at $p < 0.05$. Data are presented as the mean ± standard deviation (SD).

3. Results

3.1. The Component Analysis of Fractionated GFP

Following ethanol gradient precipitation at varying concentrations, three distinct crude polysaccharide fractions (GFP40, GFP60, and GFP80) were isolated. Quantitative analysis using the established calibration equations revealed their compositional characteristics (Table 1). Notably, GFP60 showed superior performance in both extraction yield (2.57% ± 0.2%) and total polysaccharide content (50.83% ± 1.64%), whereas GFP80 exhibited the highest protein concentration (8.46% ± 0.20%) among the fractions.

Table 1. The content of main components in different polysaccharides fractions of *Grifola frondosa*.

Items	GFP40	GFP60	GFP80
Yield	2.33 ± 0.21 ^{ab}	2.57 ± 0.20 ^{a}	2.08 ± 0.12 ^{b}
Total polysaccharide %	44.41 ± 0.96 ^{b}	50.83 ± 1.64 ^{a}	47.68 ± 3.09 ^{a}
Protein %	6.29 ± 0.22 ^{b}	8.17 ± 0.68 ^{a}	8.46 ± 0.20 ^{a}

Different superscript letters (a, b) between groups indicate statistically significant differences ($p < 0.05$); values sharing a common letter (e.g., 'ab' shares 'a' with 'a' and 'b' with 'b') do not differ significantly.

3.2. Screening of Fractionated GFP for Antioxidant and Cytoprotective Potential In Vitro

The in vitro antioxidant activity and radioprotective capacity of all crude polysaccharide fractions (GFP40, GFP60, GFP80) are shown in Figure 1. All three fractions exhibited dose-dependent ABTS radical scavenging activity, DPPH radical scavenging rate, and total reducing power. Notably, as shown in Figure 1A, when the concentration exceeded 0.01 mg/mL, GFP60 demonstrated significantly superior ABTS radical scavenging activity compared to GFP40 and GFP80. As shown in Figure 1B, distinct differences in DPPH radical scavenging rates among GFP40, GFP60, and GFP80 emerged when the sample concentration exceeded 0.25 mg/mL. GFP60 exhibited the strongest DPPH radical scavenging capacity, followed by GFP40, while GFP80 showed the weakest activity. At a final reaction concentration of 1.0 mg/mL, the scavenging rates reached 80.16% for GFP60, 49.92% for GFP40, and only 43.57% for GFP80. Notably, while GFP80 exhibited ABTS radical scavenging activity comparable to that of GFP60, its DPPH radical scavenging activity was substantially lower, ranking the lowest among the three fractions. As shown in Figure 1C, the total reducing power of GFP60 consistently surpassed that of GFP40 and GFP80 as the sample concentration increased. Therefore, GFP60 exhibited superior scavenging capabilities against above three types of free radicals.

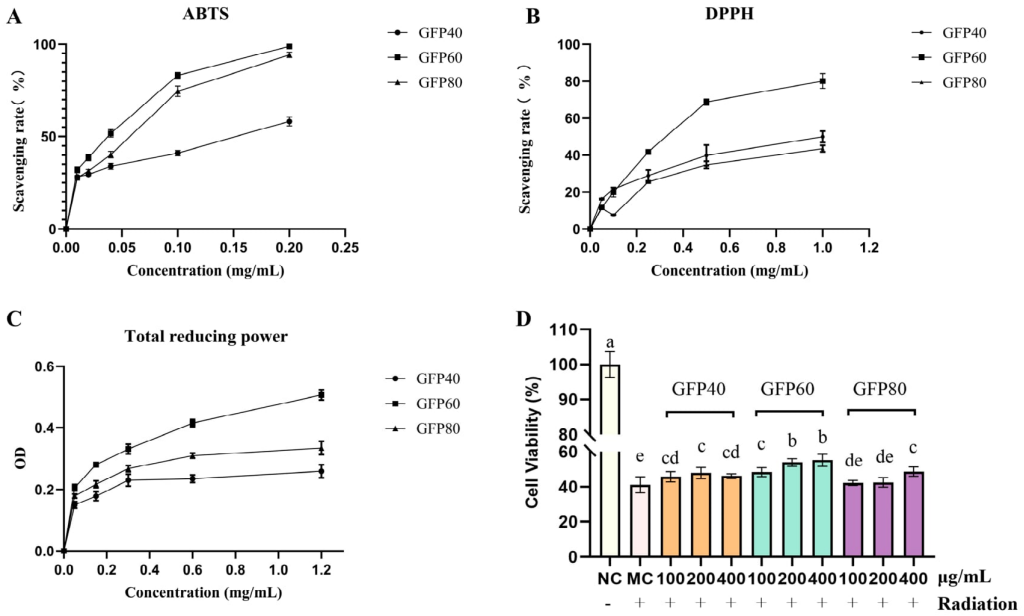


Figure 1. In vitro antioxidant activity and cell viability of different GFP fractions. ABTS radical scavenging activity (**A**). DPPH radical scavenging activity (**B**). Total reducing power assay (**C**). Radioprotective ability in macrophages (**D**). Results are expressed as mean ± SD ($n = 3$). Different letters denote significant difference at $p < 0.05$; values sharing a common letter (e.g., 'ab' shares 'a' with 'a' and 'b' with 'b') do not differ significantly.

Figure 1D displays the survival rates of macrophage in each group after radiation treatment. It can be observed that the macrophage survival rates in all groups treated with γ-radiation were lower than those in the blank control group, indicating that γ-radiation significantly damaged macrophages and reduced their survival. Pretreatment with GFP40, GFP60, and GFP80 all alleviated radiation-induced damage to different degrees. Overall, GFP60 demonstrated the most pronounced protective effect across different concentrations of 100, 200, and 400 μg/mL. Specifically, GFP60 at concentration of 400 μg/mL elevated post-irradiation macrophage survival rate to 55.12%.

In summary, GFP40, GFP60, and GFP80 exhibited antioxidant activities, with GFP60 demonstrating the superior abilities and the most effective cellular protection against radiation. Therefore, GFP60 was selected for subsequent experiments to evaluate its radiation protection effect.

3.3. GFP60 Ameliorated Physiological Health Status and Histopathological Damage in Irradiated Mice

Irradiation caused significant damage to the spleen, thymus and liver in mice (Figure 2A–C). However, the radiation-induced injury to these organs was gradually restored upon administration of GFP60. Notably, the thymus index, spleen index and liver index in the GFPH group were comparable to that in the NC group ($p > 0.05$). Radiation exposure significantly reduced body weight in the MC group, confirming the successful establishment of the acute radiation injury model (Figure 2D). Amifostine in the PC group partially reversed this effect, but body weight remained significantly lower than pre-irradiation levels ($p < 0.05$). In contrast, mice in the GFP60 groups showed no significant difference in body weight before and after irradiation ($p > 0.05$), indicating that GFP60 effectively alleviated radiation-induced weight loss.

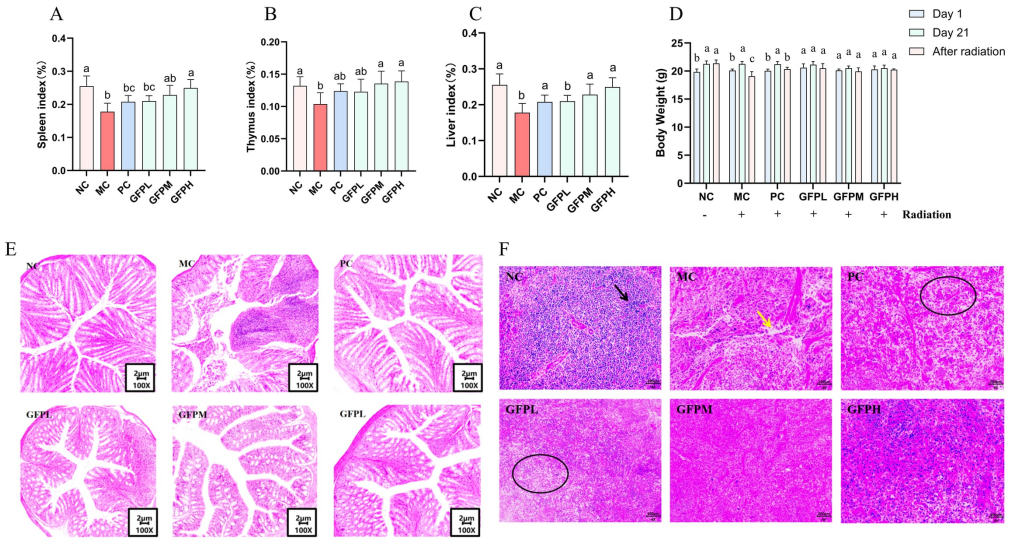


Figure 2. Effects of GFP60 on physiological indices in irradiated mice. Spleen index (**A**). Thymus index (**B**). Liver index (**C**). Body weight (**D**). Colonic (**E**) and splenic (**F**) tissue H&E staining images. The regions indicated by the arrows and circles represent the key areas of histological interest. Results are expressed as mean ± SD ($n = 8$). Different letters denote significant difference at $p < 0.05$; values sharing a common letter (e.g., 'ab' shares 'a' with 'a' and 'b' with 'b') do not differ significantly.

The colonic mucosa of mice in the NC and PC groups exhibited normal histology, with an intact mucosal layer and clearly visible crypt architecture (Figure 2E). In contrast, the MC group showed extensive neutrophil infiltration and other signs of abnormal inflammation in the colon, accompanied by blurred crypt architecture and mucosal damage, indicating that radiation caused marked intestinal injury in MC mice. After GFP60 treatment, these pathological alterations were substantially alleviated, as evidenced by clear crypt architecture, absence of obvious abnormal inflammatory infiltration, and an intact mucosa, suggesting that GFP60 may alleviate radiation-induced intestinal mucosal damage.

In mouse models of acute radiation injury, the primary focus of observation is the structure of the splenic corpuscles (white pulp) and lymphocyte density. As shown in Figure 2F, the splenic morphology in the NC group appeared normal, with abundant lymphocytes in the periarteriolar lymphoid sheaths (black arrows) and no significant histopathological changes. In contrast, the MC group exhibited diffuse necrosis (yellow arrows) and dissolution of the spleen, accompanied by a marked reduction in lymphocytes, indicating severe splenic damage. The PC and GFPL groups showed mitigated splenic injury, though regional necrosis and numerous apoptotic bodies (within black circles) were still present. Medium-dose GFP60 further reduced diffuse necrosis and significantly decreased apoptotic bodies, resulting in splenic morphology that approached normality. The GFPH group displayed splenic morphology closest to that of the normal controls, with minimal apoptotic bodies and a significant preventive effect on lymphocyte loss. These morphological observations indicate a protective effect of GFP60 against radiation-induced splenic injury.

3.4. GFP60 Enhanced Hematopoietic Function and Antioxidant Capacity in Irradiated Mice

The counts of WBC, RBC, and PLT in peripheral blood are shown in Figure 3A–C. Ionizing radiation caused significant damage to the mice's WBC, RBC, and PLT counts, with the WBC count being particularly affected. Furthermore, the intake of GFP60 significantly alleviated this damage, suggesting that GFP60 may exert radioprotective effects. Notably, the GFPM and GFPH dose groups of GFP60 demonstrated superior protective effects, indicating a dose-dependent trend in efficacy Interestingly, the RBC counts in the medium- and high-dose of GFP60 groups even exceeded those in the PC group.

The DNA content in the MC group was lower than that in the NC group, while both the PC group and GFP groups alleviated this DNA damage as shown in Figure 3D. Notably, DNA content gradually increased with increased doses of GFP60, which approached normal levels in the GFPH group.

The serum MDA levels in mice are shown in Figure 3E. The MC group exhibited the highest MDA content, while the PC group significantly suppressed MDA levels in mice. Although GFP60 demonstrated a weaker capacity of reducing MDA compared to the PC group, pretreatment with GFP60 still significantly lowered serum MDA levels compared to the MC group ($p < 0.05$). Specifically, high-dose GFP60 treatment reduced the serum MDA concentration to 8.03 ± 0.60 nmol/L. Figure 3F,G illustrate the antioxidant capacity of GFP60 in mice. Compared with the NC group, the MC group showed significantly reduced levels of SOD and GSH-Px ($p < 0.05$), while the PC group showed that the mice's defense capacity was significantly restored. After treatment with GFP60, both SOD and GSH-Px levels were restored in a concentration-dependent manner.

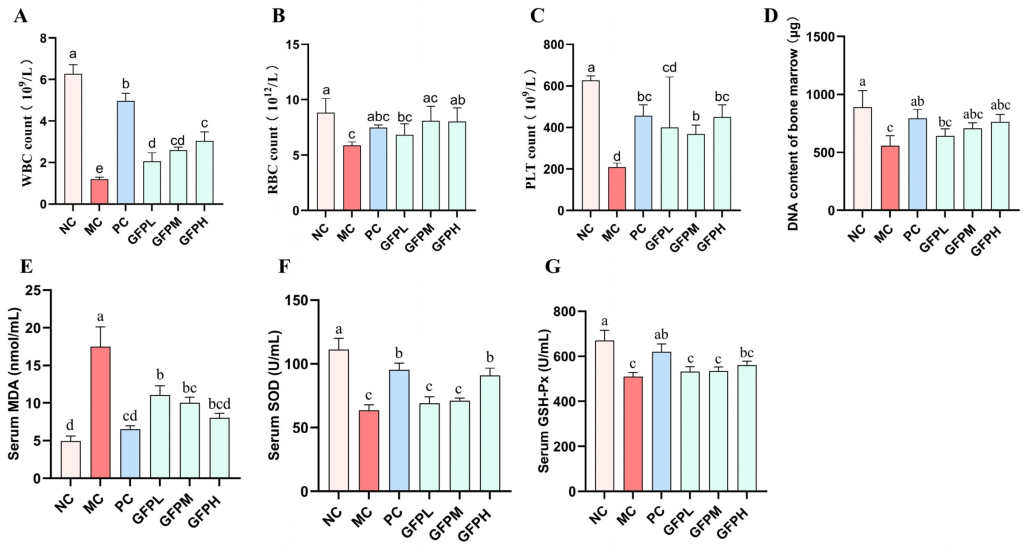


Figure 3. Blood counts of WBCs (**A**), RBCs (**B**), and PLTs (**C**). DNA content in mouse bone marrow (**D**). Levels of MDA (**E**), SOD (**F**), and GSH-Px (**G**) in serum of mice among different groups. Results are expressed as mean ± SD with $n = 5$ for WBCs, RBCs and PLTs; $n = 3$ for DNA, SOD, MDA, and GSH-PX. Different letters denote significant difference at $p < 0.05$; values sharing a common letter (e.g., 'ab' shares 'a' with 'a' and 'b' with 'b') do not differ significantly. For Figure 3C (PLT), due to the heterogeneity of variance, Welch's ANOVA followed by Tamhane's T2 post hoc test was applied for multiple comparisons. WBC: White blood cell. RBC: Red blood cell. PLT: Platelet. MDA: Malondialdehyde. SOD: Superoxide dismutase. GSH-Px: Glutathione peroxidase.

3.5. GFP60 Promoted Functional Recovery of the Immune System After Radiation

As shown in Figure 4A–C, radiation exposure significantly reduced serum levels of IgA, IgM, and IgG in mice. However, pretreatment with GFP60, particularly in the GFPM and GFPH groups, markedly elevated these immunoglobulin concentrations, which were significantly higher than those in the MC group and even approached levels observed in the PC group.

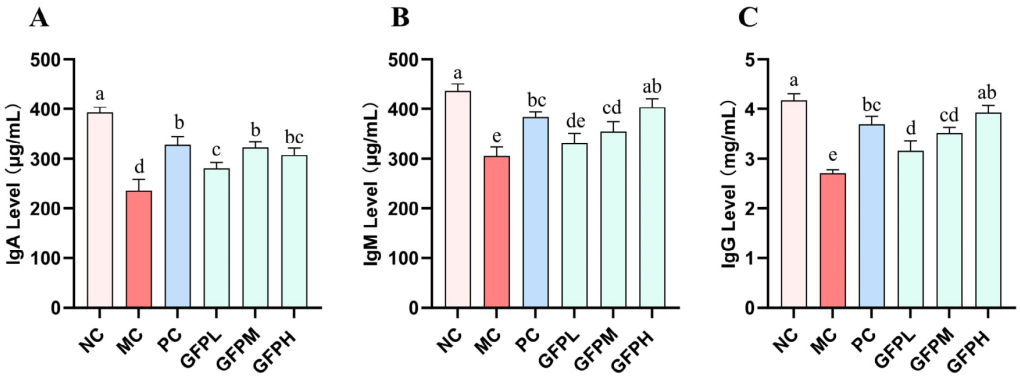


Figure 4. Effects of GFP60 on immune function in radiation-damaged mice. Levels of IgA (**A**), IgM (**B**), and IgG (**C**) in serum. Results are expressed as mean ± SD ($n = 3$). Different letters denote significant difference at $p < 0.05$; values sharing a common letter (e.g., 'ab' shares 'a' with 'a' and 'b' with 'b') do not differ significantly.

3.6. GFP60 Reshaped the Gut Microbiota in Irradiated Mice

A total of 2164 amplicon sequence variants (ASVs) were identified by 16S rRNA gene sequencing. The number of ASVs in each group was as follows: 452 in the NC group, 397 in the MC group, 401 in the PC group, and 490, 520, and 416 in the GFPL, GFPM, and GFPH groups, respectively (Figure 5A). A total of 322 ASVs were shared among all groups (Figure 5B). Compared with the NC group, the ASV count in the MC group was reduced, indicating that radiation exposure decreased gut microbial diversity. Administration of GFP60 at different doses increased ASV counts to varying degrees, suggesting that GFP60 may alleviated radiation-induced gut microbiota alterations. Notably, the ASV count in the GFPH group was lower than that in the GFPL group, with the GFPM group showing the highest value, indicating that the optimal modulatory effect on ASV richness was achieved at the GFPM group in this study.

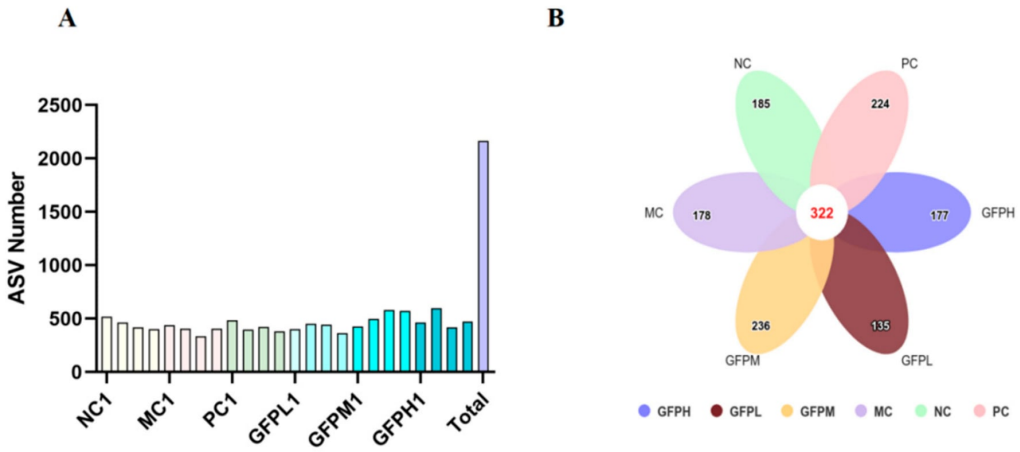


Figure 5. The effect of GFP60 on ASV of the intestinal flora of radiation-damaged mice; (**A**) graph of the number of OTUs per sample, (**B**) Venn diagram based on ASVs. Results are expressed as mean ± SD ($n = 4$).

Figure 6 illustrates the effect of GFP60 on the α-diversity of the gut microbiota in irradiated mice. Compared with the NC group, radiation exposure decreased the Chao1 and Shannon indices in the MC group. In contrast, these indices were significantly increased in the GFP60-treated groups. Notably, the Chao1 and Shannon indices in the GFPM group showed highly significant differences compared with the MC group ($p < 0.01$) (Figure 6A,B). Conversely, radiation elevated the Simpson index in mice, while GFP60 intake alleviated this increase (Figure 6C).

As the number of sequenced species increased, both the rarefaction curve (Figure 6D) and Shannon index curve (Figure 6E) plateaued, indicating that the sequencing depth was sufficient to capture the majority of the microbial diversity. When the sample size reached 24, the species accumulation curve leveled off, suggesting that the sequencing library size was adequate and the data were reliable (Figure 6F). Furthermore, the rank abundance curve (Figure 6G) illustrates the compositional differences among samples: compared with the NC group, radiation exposure reduced species richness (narrower curve width) and altered species evenness (steeper curve slope), whereas GFP60 treatment partially restored these parameters.

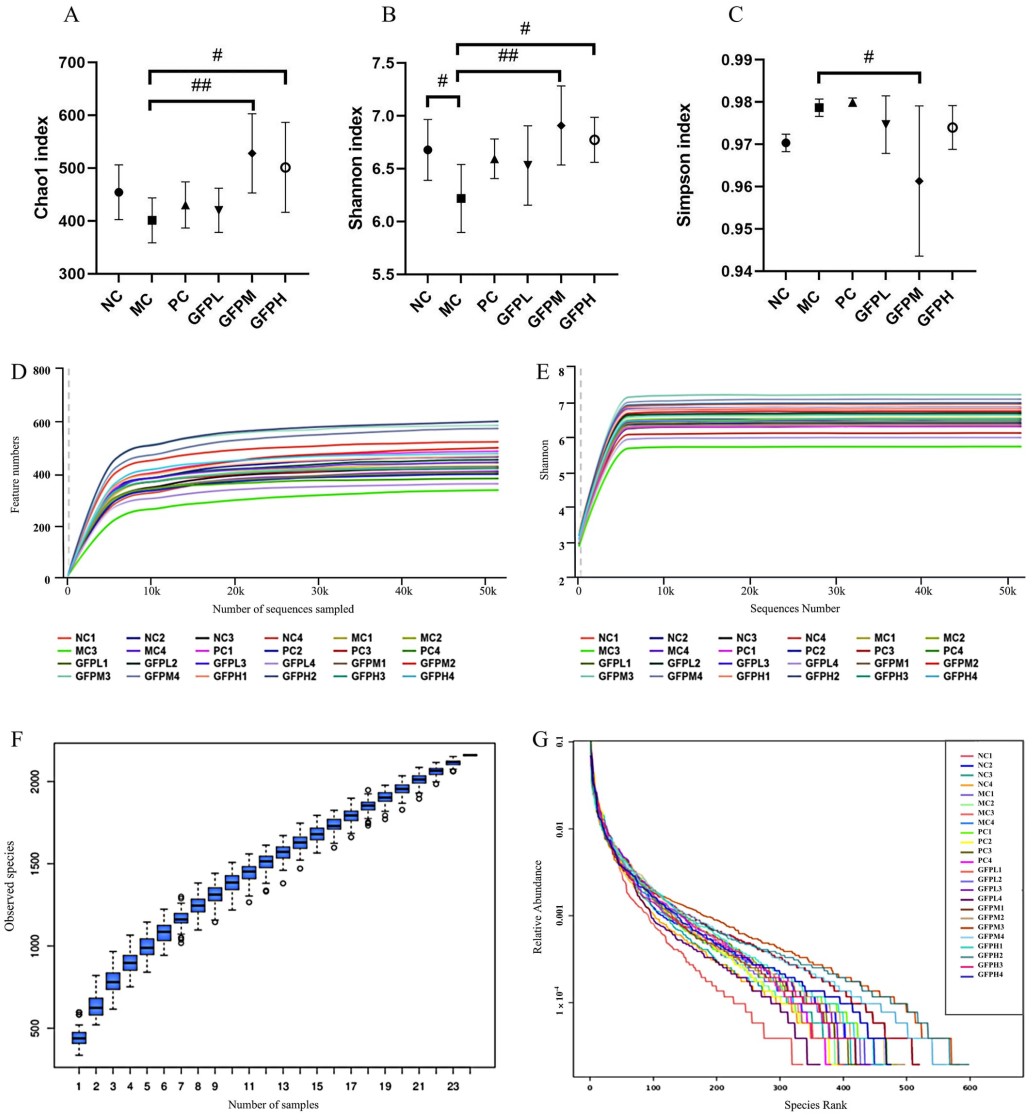


Figure 6. The effect of GFP60 on the alpha diversity of intestinal flora of radiation-damaged mice. (**A**) Chao1 index. (**B**) Shannon index. (**C**) Simpson index. (**D**) Dilution plot. (**E**) Fragrance index curve. (**F**) Species accumulation curve. (**G**) Rank abundance curve. Results are expressed as mean ± SD, with $n = 3$ for Chao 1 and $n = 4$ for Shannon and Simpson. # denotes a statistically significant difference between groups ($p < 0.05$), while ## denotes a highly significant difference ($p < 0.01$).

As shown in Figure 7A, in the PCoA plot, most NC group samples clustered in the lower-left region, while MC group samples were predominantly located in the lower-right region, distant from the NC group. This spatial distribution indicates that radiation exposure altered the gut microbiota composition in MC mice. In contrast, the GFPM and GFPH groups showed closer proximity to the NC group in the PCoA plot, suggesting that GFP60 administration improved the gut microbiota profile. Further analysis of NMDS (Figure 7B) yielded results consistent with the PCoA findings. UPGMA clustering analysis (Figure 7C) revealed substantial separation between NC and MC groups, reflecting the pronounced impact of radiation on the microbial community. The GFPL group clustered closely with the MC group, indicating minimal improvement in gut microbiota with low-dose treatment. However, GFPM and GFPH groups demonstrated marked restorative effects, forming distinct branches nearest to the NC group, which indicates substantial recovery of gut microbiota composition following medium- and high-dose GFP60 administration.

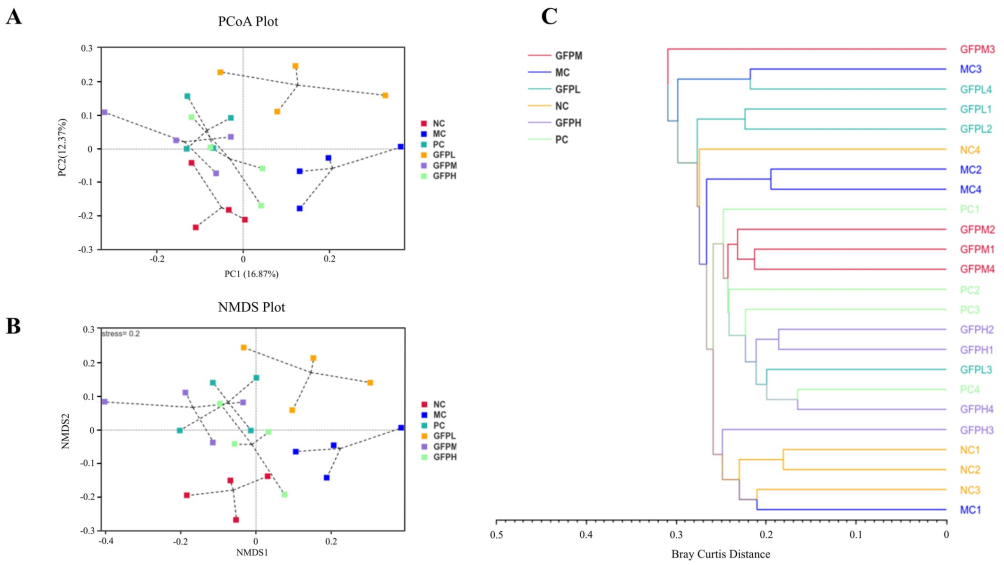


Figure 7. Beta diversity of intestinal microbiota in radiation-injured mice treated with GFP60. (**A**) Bray–Curtis-based PCoA plot; (**B**) Bray–curtis-based NMDS plot; (**C**) UPGMA dendrogram based on bray–curtis distance. Results are expressed as mean ± SD ($n = 4$). PCoA plot: principal coordinate analysis plot; NMDS plot: non-metric multidimensional scaling plot; UPGMA: unweighted pair-group method with arithmetic mean.

As shown in Figure 8A,B, at the phylum level, *Bacteroidota* and *Firmicutes* were the two most abundant phyla across all groups. Compared with the NC group, the MC group exhibited an increased relative abundance of *Bacteroidota* (Figure 8E) and a decreased relative abundance of *Firmicutes* (Figure 8F). However, treatment with GFP60 significantly attenuated these changes, restoring the relative abundances of both phyla to levels comparable to those of the NC group. At the genus level (Figure 8C,D), *Bacteroides*, *Lachnospiraceae_NK4A136_group*, and *Alistipes* were the three most abundant genera. Compared with the NC group, radiation exposure significantly increased the relative abundance of Bacteroides while decreasing that of *Lachnospiraceae_NK4A136_group* and *Alistipes* (Figure 8G–I). The GFPM group significantly reduced the radiation-induced increase in Bacteroides abundance ($p < 0.01$), whereas the GFPL group significantly attenuated the reduction in *Lachnospiraceae_NK4A136_group* abundance ($p < 0.05$).

Figure 9 shows the characteristic differentially abundant microbial taxa in each group identified by linear discriminant analysis effect size (LEfSe) analysis. At the class level, *Campylobacteria* in the NC group, *Desulfovibrionia* in the MC group, *Saccharimonadia* in the GFPM group, and *Alphaproteobacteria* in the GFPL group were the most differentially abundant taxa compared to other groups. At the order level, *Campylobacterales* (NC group), *Desulfovibrionales* (MC group), *Clostridia_UCG_014*, *Clostridia_vadinBB60_group*, and *Saccharimonadales* (GFPM group), as well as *Rhodospirillales* (GFPL group), exhibited the most significant differences compared to other groups. Additionally, at the family level, *Tannerellaceae* and *Desulfovibrionaceae* in the MC group and *Saccharimonadaceae* in the GFPM group were the most differentially significant taxa compared to other groups. The LEfSe analysis visualization revealed that the gut microbiota structure of irradiated mice exhibited certain intergroup differences compared to the NC group. Compared with the MC group, the microbial composition in the GFPL and GFPH groups showed some reduction.

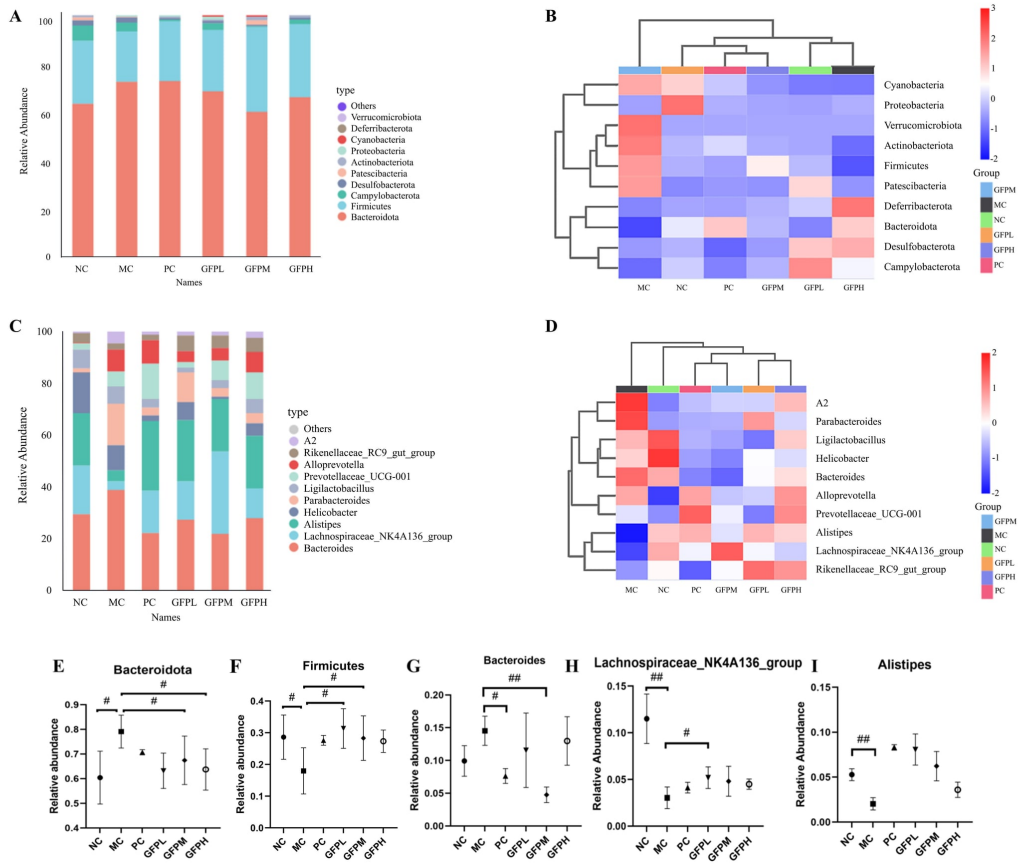


Figure 8. The effect of GFP60 on the phylum and genus levels of intestinal flora of radiation-damaged mice. (**A**) Phylum-level abundance map. (**B**) Phylum-level heat map. (**C**) Genus-level abundance map. (**D**) Genus-level heat map. (**E**–**I**) Significance analysis of flora abundance. Results are expressed as mean ± SD ($n = 4$). # denotes a statistically significant difference between groups ($p < 0.05$), while ## denotes a highly significant difference ($p < 0.01$).

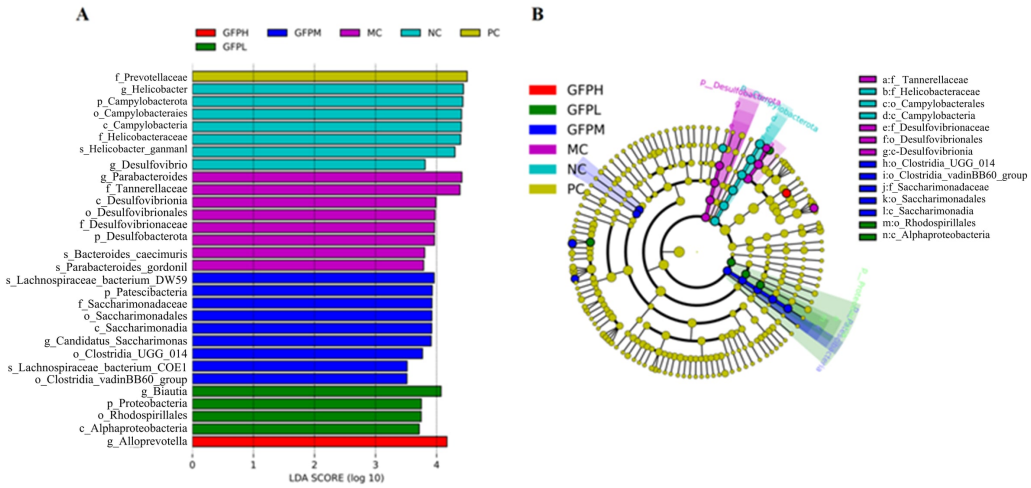


Figure 9. Inter-group differences in gut microbiota of irradiated mice treated with GFP60. (**A**) Histogram of the distribution of LDA values of different flora. (**B**) Evolutionary branching of different flora. Results are expressed as mean ± SD ($n = 4$). LDA-SCORE: Linear discriminant analysis score.

4. Discussion

Ionizing radiation causes damage primarily through the overproduction of reactive oxygen species (ROS), which induces oxidative injury to cellular macromolecules [31]. Based on this mechanism, compounds with free radical scavenging capacity are considered promising candidates for radioprotection. Thus, the radical scavenging activity of GFP serves as an initial indicator of its radioprotective potential. Meanwhile, the effectiveness of a radioprotective agent is closely related to its capacity to maintain cell viability after irradiation. Accordingly, the macrophage survival assay was used to evaluate the cytoprotective effects of the polysaccharides at the cellular level. It has been reported that polysaccharides precipitated by low-concentration ethanol typically possess higher molecular weights and more complex structures, whereas those obtained at higher ethanol concentrations generally exhibit lower molecular weights [32]. By combining in vitro antioxidant activity with cytoprotective efficacy, three crude fractionated polysaccharides were compared, and GFP60 was identified as the most promising candidate for further in vivo investigation.

In the ABTS and DPPH radical scavenging assays, GFP60 exhibited superior scavenging capacity compared to GFP40 and GFP80. Although the ABTS activity of GFP80 was comparable to that of GFP60, its DPPH activity was substantially lower. Previous studies have demonstrated that the divergent antioxidant performance of polysaccharides in ABTS (predominantly single electron transfer) and DPPH (predominantly hydrogen atom transfer) systems is often attributed to their structural features, such as uronic acid content and glycosidic linkage types [33]. Therefore, we speculate that the discrepancies observed between GFP80 and GFP60 in our study may be attributable to differences in their uronic acid content or glycosidic linkage types, which could lead to distinct electron-donating and hydrogen atom-donating capacities.

GFP60 ameliorated pathological symptoms in irradiated mice, including weight loss, intestinal and splenic damage, and organ atrophy. As central organs of the immune system, the spleen and thymus are responsible for the generation and maturation of immune cells, which are highly susceptible to radiation-induced damage [34]. Consistent with this, previous studies have shown that other natural compounds, such as 10-hydroxydec-2-enoic acid (10-HAD), can restore the immune function of the thymus and spleen in immunosuppressed mice by promoting lymphocyte proliferation and differentiation [35]. Similarly, our results suggest that the protection of splenic and thymic tissues by GFP60 may contribute to the restoration of humoral immunity.

The intestinal epithelium and spleen are enriched with rapidly dividing cells that are highly sensitive to radiation [36,37]. Notably, colonic crypts are widely recognized as a key indicator for evaluating acute radiation injury, as radiation directly eliminates the stem cells located at the base of the crypts, leading to crypt loss and cellular apoptosis [38]. Histological findings from the present study indicated that GFP60 significantly attenuated radiation-induced colonic and splenic damage at the morphological level. These observations align with previous reports showing that natural polysaccharides can mitigate radiation-induced tissue lesions [39].

Excessive free radicals induced by radiation can directly attack the polyunsaturated fatty acids in cell membranes, triggering a lipid peroxidation chain reaction and ultimately generating MDA—a widely recognized biomarker for assessing the severity of oxidative stress damage [40]. Concurrently, these free radicals excessively consume and damage the endogenous antioxidant enzymes SOD and GSH-Px, leading to a marked decline in their activities [41–43]. SOD and GSH-Px act synergistically to convert harmful free radicals into harmless water [44]. GFP60 restored the activities of SOD and GSH-Px, consistent with previous findings that *Grifola frondosa* polysaccharides can enhance endogenous antioxidant

defense systems in hepatic fibrosis in rats [45]. Collectively, these findings indicate that GFP60 may contribute to the alleviation of radiation-induced oxidative stress.

Excessive free radicals induced by radiation can directly attack the DNA of bone marrow hematopoietic stem cells, leading to DNA double-strand breaks and apoptosis. Therefore, bone marrow DNA content serves as a valuable indicator for assessing the degree of radiation-induced damage [46,47]. The protective effect of *Laminaria japonica* polysaccharide against radiation-induced DNA damage was indirectly verified by assessing the expression of phosphorylated histone H2AX (γ-H2AX) [48]. Under the same radiation dose, different blood cells exhibit marked differences in radiation sensitivity. WBCs, particularly lymphocytes, have a short lifespan and high proliferative activity, making them the earliest and most dramatically declining cell population after irradiation, followed by PLTs, while RBCs, having the longest lifespan, are affected last [49]. Our findings suggest that GFP60 may scavenge excessive radiation-induced reactive oxygen species in vivo, thereby potentially protecting hematopoietic stem cell DNA from oxidative damage, and maintaining their normal proliferation and differentiation capacity, which may collectively contribute to the recovery of peripheral blood cell counts. These results highlight the potential of GFP60 as a novel radioprotective agent in supporting hematopoietic function.

Humoral immunity is a key defense mechanism whereby the body produces immunoglobulins to combat pathogens such as bacteria and viruses [50]. IgA, IgM, and IgG represent the three most predominant and abundant antibody classes in humoral immunity, and their concentration levels directly reflect the functional strength of this humoral immunity [51]. Radiation exposure significantly reduced serum levels of IgA, IgM, and IgG in mice, indicating radiation-induced immunosuppression [52]. GFP60 treatment significantly increased the serum levels of immunoglobulins (IgA, IgM, and IgG) in irradiated mice, consistent with previous studies demonstrating that GFP60 can enhance serum immunoglobulin levels in a cyclophosphamide-induced intestinal injury model [53].

GFP60 increased the abundance of ASVs, and modulated the α-diversity of gut microbiota, suggesting that GFP60 may alleviate radiation-induced gut microbiota alterations. The Chao 1 index reflects community richness, while the Shannon and Simpson indices consider both richness and evenness—i.e., whether the proportions of different bacterial species are balanced. A higher Shannon index combined with a lower Simpson index indicates greater community diversity [54]. PCoA plots showed that GFP60 intake shifted the β-diversity of gut microbiota in irradiated mice closer to that of the NC group.

Consistent with previous reports [55,56], radiation exposure in this study significantly increased the relative abundance of *Bacteroides* while decreasing that of *Lachnospiraceae_NK4A136_group* in mice, and GFP60 treatment effectively attenuated these changes, restoring the gut microbiota composition toward that of the NC group. *Lachnospiraceae_NK4A136_group* is recognized as one of the known short-chain fatty acid (SCFA)-producing bacterial taxa [57]. The recovery of its abundance following GFP60 treatment suggests that GFP60 may promote SCFA production. whether this shift contributes to the maintenance of intestinal barrier integrity and the reduction in LPS translocation remains to be verified. At the genus level, GFP60 increased the abundance of beneficial bacteria such as *Alistipes* in mice. This result is consistent with the effects of the total active components of *Grifola frondosa* in alleviating gut microbiota dysbiosis in alcohol-fed mice [58]. In the present study, GFP60 treatment significantly increased the abundance of *Alistipes*, accompanied by a marked restoration of serum SOD and GSH-Px activities. This is consistent with previous reports showing a positive correlation between Alistipes abundance and antioxidant enzyme activities [59], suggesting that the increased abundance of Alistipes may be partially associated with the antioxidant protective effects of GFP60.

Despite these promising results, this study has several limitations. First, GFP60 is a crude polysaccharide fraction that may contain residual proteins and other uncharacterized components. These components could also contribute, at least in part, to the observed biological effects; therefore, the effects reported here should be attributed to the tested fraction as a whole rather than to any single purified polysaccharide. Second, the monosaccharide composition and molecular weight distribution of GFP60 were not determined. Third, while we observed protective effects, the precise molecular mechanisms (e.g., specific signaling pathways or receptor interactions) were not directly validated.

In summary, GFP60 may exert its radioprotective effects through a potential multi-target mechanism (Figure 10). By alleviating radiation-induced oxidative stress, GFP60 may protect DNA from free radical attack, thereby potentially preserving the viability and function of WBC, RBC and PLT. Concurrently, it may restore humoral immunity, as reflected by elevated immunoglobulin levels. These combined actions may contribute to the maintenance of body weight and organ indices, indicating overall recovery. In parallel, GFP60 may remodel the gut microbiota composition, which may further reinforce the overall protective efficacy. Collectively, these findings suggest that GFP60 attenuate radiation-induced injury potentially involving regulation of oxidative stress, hematopoietic function, immune defense, and gut microbial homeostasis.

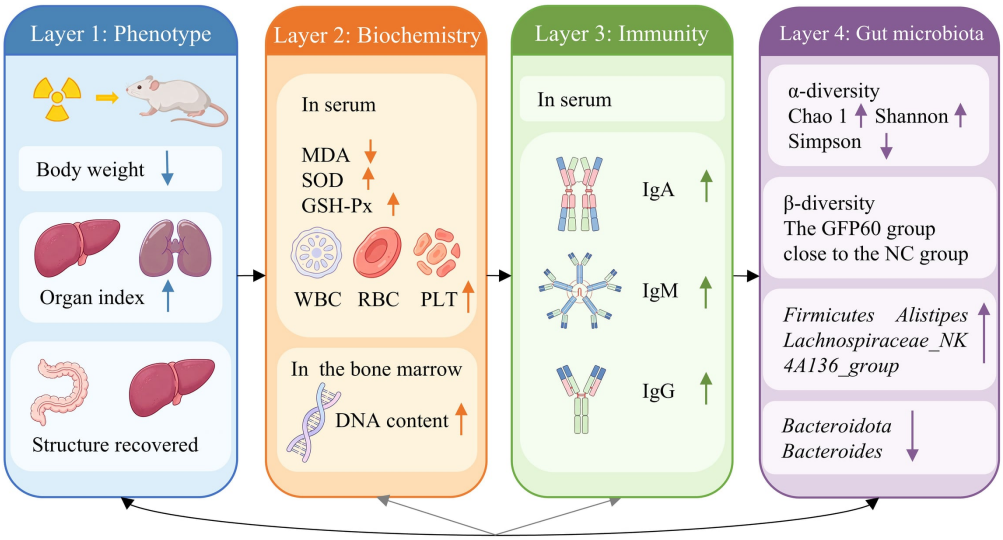


Figure 10. Mechanism diagram of the radioprotective effects of GFP60. The arrows (↑ and ↓) indicate an increase and decrease in the indicators, respectively.

5. Conclusions

In this study, GFP60 was prepared from *Grifola frondosa* polysaccharides. Our results suggest that GFP60 may attenuate radiation-induced injury, potentially through reducing serum oxidative stress markers, protecting DNA integrity, enhancing humoral immunity, and remodeling gut microbial diversity. Overall, this study provides experimental evidence for the potential application of GFP60 in radiation protection and lays a foundation for the development of a novel natural radioprotective agent.

Author Contributions: Conceptualization, X.Z. and K.Y.; methodology, S.Z.; software, M.S.; validation, S.Z. and M.S.; formal analysis, M.S.; investigation, S.Z.; resources, G.J.; data curation, S.Z. and M.S.; writing—original draft preparation, S.Z.; writing—review and editing, X.Z.; visualization, P.S. and G.F.; supervision, K.Y.; project administration, K.Y.; funding acquisition, K.Y. and H.C. All authors have read and agreed to the published version of the manuscript.

Funding: This research was funded by the Zhejiang Province Key Research and Development Program (No. 2025C01101 and 2025C04031), the Project of Zhejiang Provincial Department of Agriculture and Rural Affairs (No. 2026SNJF091 and 2025SNJF023), the National Natural Science Foundation of China (No. 32302016), and the Zhejiang Provincial Natural Science Foundation (No. LQ24C200012).

Institutional Review Board Statement: The animal study protocol was approved by the Ethics Committee of Zhejiang Academy of Agricultural Sciences (Approval No. 25ZALAS44; 18 July 2025).

Informed Consent Statement: Not applicable.

Data Availability Statement: The original contributions presented in this study are included in the article. Further inquiries can be directed to the corresponding author.

Conflicts of Interest: Author Guohua Ji was employed by the company Hangzhou Huaxian High-Tech Co., Ltd. Author Guofu Feng was employed by the company Zhejiang Jolly Pharmaceutical Co., Ltd. The remaining authors declare that the research was conducted in the absence of any commercial or financial relationships that could be construed as a potential conflict of interest.

Abbreviations

The following abbreviations are used in this manuscript:

GFP	*Grifola frondosa* polysaccharide
10-HAD	10-hydroxydec-2-enoic acid
ABTS	2,2′-azino-bis (3-ethylbenzothiazoline-6-sulfonic acid)
ANOVA	One-way analysis of variance
ASVs	Amplicon sequence variants
BSA	Bovine serum albumin
CCK-8	Cell counting kit-8
DPPH	2,2-diphenyl-1-picrylhydrazyl
EDTA	Ethylenediaminetetraacetic acid
EP	Eppendorf
FLASH	Fast length adjustment of short reads
GSH-Px	Glutathione peroxidase
IgA	Immunoglobulin A
IgG	Immunoglobulin G
IgM	Immunoglobulin M
LDA-SCORE	Linear discriminant analysis score
LEfSe	Linear discriminant analysis effect size
LPS	Lipopolysaccharide
MDA	Malondialdehyde
MDS	Multi-dimensional scaling
NMDS	Non-metric multidimensional scaling
OTUs	Operational taxonomic units
PCoA	Principal coordinate analysis
PCR	Polymerase chain reaction
PLT	Platelet
QIIME	Quantitative insights into microbial ecology
RBC	Red blood cell
ROS	Reactive oxygen species
SD	Standard deviation
SOD	Superoxide dismutase
SPF	Specific pathogen-free
UPGMA	Unweighted pair-group method with arithmetic mean
WBC	White blood cell
γ-H2AX	Phosphorylated histone H2AX

References

1. Talapko, J.; Talapko, D.; Katalinić, D.; Kotris, I.; Erić, I.; Belić, D.; Vasilj Mihaljević, M.; Vasilj, A.; Erić, S.; Flam, J.; et al. Health Effects of Ionizing Radiation on the Human Body. *Medicina* **2024**, *60*, 653. [CrossRef] [PubMed]
2. Dainiak, N. Hematologic consequences of exposure to ionizing radiation. *Exp. Hematol.* **2002**, *30*, 513–528. [CrossRef] [PubMed]

3. Tian, M.; Ding, X.; Pang, Y.; Xu, D.; Sun, Y.; Xia, P. Transcriptomic dose-response by UVC and heavy ion radiation reveal pathways to immune impairment. *Toxicol. In Vitro* **2025**, *108*, 106086. [CrossRef] [PubMed]
4. Yousif, A.E.; Abdelgawad, M.H.; Kamal, K.A.; Ibrahim, I.H.; Talaat, M.S.; Desouky, O.S. Dose dependent immune and antioxidant in responses to low dose radiation. *Appl. Radiat. Isot.* **2026**, *238*, 112964. [CrossRef] [PubMed]
5. Liu, S.-Z. Nonlinear dose-response relationship in the immune system following exposure to ionizing radiation: Mechanisms and implications. *Nonlinearity Biol. Toxicol. Med.* **2003**, *1*, 71–92. [CrossRef] [PubMed]
6. Banerjee, S.; Fu, Q.; Shah, S.K.; Melnyk, S.B.; Sterneck, E.; Hauer-Jensen, M.; Pawar, S.A. C/EBPδ protects from radiation-induced intestinal injury and sepsis by suppression of inflammatory and nitrosative stress. *Sci. Rep.* **2019**, *9*, 13953. [CrossRef] [PubMed]
7. Somosy, Z.; Horvath, G.; Telbisz, A.; Rez, G.; Palfia, Z. Morphological aspects of ionizing radiation response of small intestine. *Micron* **2002**, *33*, 167–178. [CrossRef] [PubMed]
8. Quillen, E.E.; Schaaf, G.W.; Justice, J.N.; Dugan, G.O.; Johnson, B.; Reed, C.; Olson, J.D.; Cline, J.M. Widespread Multimorbidity in a Cohort of Aging, Radiation-exposed Rhesus Macaques. *Radiat. Res.* **2025**, *204*, 283–293. [CrossRef] [PubMed]
9. Chino, Y.; Olson, J.D.; Aichele, S.; Bailey, S.M.; Schaaf, G.W.; Cline, J.M.; Johnson, T.E. The Impact of Dose, Sex, and Age at Time of Acute Whole-body Radiation Exposure on Long-term Hematopoiesis in Rhesus Macaques (*Macaca mulatta*). *Radiat. Res.* **2025**, *204*, 408–420. [CrossRef] [PubMed]
10. Yi, J.; Zhu, J.; Zhao, C.; Kang, Q.; Zhang, X.; Suo, K.; Cao, N.; Hao, L.; Lu, J. Potential of natural products as radioprotectors and radiosensitizers: Opportunities and challenges. *Food Funct.* **2021**, *12*, 5204–5218. [CrossRef] [PubMed]
11. Wang, W.; Xue, C.; Mao, X. Radioprotective effects and mechanisms of animal, plant and microbial polysaccharides. *Int. J. Biol. Macromol.* **2020**, *153*, 373–384. [CrossRef] [PubMed]
12. He, X.; Wang, X.; Fang, J.; Chang, Y.; Ning, N.; Guo, H.; Huang, L.; Huang, X.; Zhao, Z. Polysaccharides in *Grifola frondosa* mushroom and their health promoting properties: A review. *Int. J. Biol. Macromol.* **2017**, *101*, 910–921. [CrossRef] [PubMed]
13. Yang, W.; Wu, J.; Liu, W.; Ai, Z.; Cheng, Y.; Wei, Z.; Zhang, H.; Ma, H.; Cui, F.; Zhou, C.; et al. Structural characterization, antioxidant and hypolipidemic activity of *Grifola frondosa* polysaccharides in novel submerged cultivation. *Food Biosci.* **2021**, *42*, 101187. [CrossRef]
14. Yu, J.; Ji, H.-y.; Liu, C.; Liu, A.-j. The structural characteristics of an acid-soluble polysaccharide from *Grifola frondosa* and its antitumor effects on H22-bearing mice. *Int. J. Biol. Macromol.* **2020**, *158*, 1288–1298. [CrossRef] [PubMed]
15. Seo, Y.R.; Patel, D.K.; Shin, W.C.; Sim, W.S.; Lee, O.H.; Lim, K.T. Structural Elucidation and Immune-Enhancing Effects of Novel Polysaccharide from *Grifola frondosa*. *Biomed. Res. Int.* **2019**, *2019*, 7528609. [CrossRef] [PubMed]
16. Guo, W.L.; Deng, J.C.; Pan, Y.Y.; Xu, J.X.; Hong, J.L.; Shi, F.F.; Liu, G.L.; Qian, M.; Bai, W.D.; Zhang, W.; et al. Hypoglycemic and hypolipidemic activities of *Grifola frondosa* polysaccharides and their relationships with the modulation of intestinal microflora in diabetic mice induced by high-fat diet and streptozotocin. *Int. J. Biol. Macromol.* **2020**, *153*, 1231–1240. [CrossRef] [PubMed]
17. He, Y.; Zhang, L.; Wang, H. Chapter Eleven—The biological activities of the antitumor drug *Grifola frondosa* polysaccharide. In *Progress in Molecular Biology and Translational Science*; Zhang, L., Ed.; Academic Press: Cambridge, MA, USA, 2019; Volume 163, pp. 221–261.
18. Wu, J.; Shen, W.; Tao, W.; Fan, J.; Xiang, H.; Khan, A.; Sui, B.; Zhang, X.; Wang, W.; Sun, X.; et al. Characterization of the gel-binding mechanism of *Grifola frondosa* polysaccharide and polymerized whey protein by simultaneous rheology and Fourier-transform infrared spectroscopy and its application in yogurt. *J. Dairy Sci.* **2026**, *109*, 3318–3336. [CrossRef] [PubMed]
19. Tian, B.; Zhou, X.; Geng, Y.; Hu, J.; Ye, B.; Sun, P.; Yang, K. Characterization and in vitro digestion of alkali-extracted polysaccharides from *Grifola frondosa* and its impacts on human gut microbiota. *Food Biosci.* **2024**, *60*, 104499. [CrossRef]
20. Meng, M.; Cheng, D.; Han, L.; Chen, Y.; Wang, C. Isolation, purification, structural analysis and immunostimulatory activity of water-soluble polysaccharides from *Grifola frondosa* fruiting body. *Carbohydr. Polym.* **2017**, *157*, 1134–1143. [CrossRef] [PubMed]
21. Tan, G.; Duan, Z.; Xia, G.; Xin, T.; Yang, L.; Liu, F.; Xie, H. Ultrasonic-Assisted Extraction and Gastrointestinal Digestion Characteristics of Polysaccharides Extracted from *Mallotus oblongfolius*. *Foods* **2024**, *13*, 1799. [CrossRef] [PubMed]
22. Khan, A.A.; Yao, F.-J.; Cui, F.-J.; Li, Y.; Lu, L.; Khan, I.; Jalal, A.; Fang, M.; Alabbosh, K.F.; Awad, M.F.; et al. Comparative analysis of physicochemical properties and biological activities of crude polysaccharides isolated from selected Auricularia cornea strains. *Food Biosci.* **2024**, *60*, 104486. [CrossRef]
23. Lu, Y.; Fu, T.-J. Performance of Commercial Colorimetric Assays for Quantitation of Total Soluble Protein in Thermally Treated Milk Samples. *Food Anal. Methods* **2020**, *13*, 1337–1345. [CrossRef]
24. Engin, T.; Çiğdem, A.; Alma, M.H.; Alwazeer, D. Hydrogen-rich solvent method enhances the extraction of phenolics, pigments, reducing sugars, organic acids, and vitamin C from cowslip (*Primula veris* L.) flower. *Food Chem.* **2025**, *463*, 141271. [CrossRef] [PubMed]
25. Bai, Z.; Tang, J.; Li, Y.; Li, Z.; Gu, S.; Deng, L.; Zhang, Y. Integrated Metabolomics Approach Reveals the Dynamic Variations of Metabolites and Bioactivities in Paeonia ostii 'Feng Dan' Leaves during Development. *Int. J. Mol. Sci.* **2024**, *25*, 1059. [CrossRef] [PubMed]

26. Mohammed, E.A.; Abdalla, I.G.; Alfawaz, M.A.; Mohammed, M.A.; Al Maiman, S.A.; Osman, M.A.; Yagoub, A.E.A.; Hassan, A.B. Effects of Extraction Solvents on the Total Phenolic Content, Total Flavonoid Content, and Antioxidant Activity in the Aerial Part of Root Vegetables. *Agriculture* **2022**, *12*, 1820. [CrossRef]
27. Li, Q.; Zhao, T.; Mao, G.; Feng, W.; Chen, Y.; Zou, T.; Yang, L.; Qian, J.-Y. A Se-enriched *Grifola frondosa* polysaccharide induces macrophage activation by TLR4-mediated MAPK signaling pathway. *Int. J. Biol. Macromol.* **2023**, *238*, 124108. [CrossRef] [PubMed]
28. Shi, J.; Guo, J.; Chen, L.; Ding, L.; Zhou, H.; Ding, X.; Zhang, J. Characteristics and anti-radiation activity of different molecular weight polysaccharides from *Potentilla anserina* L. *J. Funct. Foods* **2023**, *101*, 105425. [CrossRef]
29. Jiang, S.; Shen, X.; Liu, Y.; He, Y.; Jiang, D.; Chen, W. Radioprotective effects of Sipunculus nudus L. polysaccharide combined with WR-2721, rhIL-11 and rhG-CSF on radiation-injured mice. *J. Radiat. Res.* **2015**, *56*, 515–522. [CrossRef] [PubMed]
30. Guo, J.; Yang, H.; Liu, Y.; Liu, W.; Zhao, R.; Li, H.; Long, W.; Xu, W.; Guo, M.; Zhang, X. Atomically precise silver clusterzymes protect mice from radiation damages. *J. Nanobiotechnology* **2021**, *19*, 377. [CrossRef] [PubMed]
31. Spitz, D.R.; Hauer-Jensen, M. Ionizing Radiation-Induced Responses: Where Free Radical Chemistry Meets Redox Biology and Medicine. *Antioxid. Redox Signal.* **2014**, *20*, 1407–1409. [CrossRef] [PubMed]
32. Wang, X.; Zhang, J.; Zhang, K.; Guo, Z.; Xu, G.; Huang, L.; Wang, L.; Li, J. Ultrasound-Assisted Enzyme Extraction, Physicochemical Properties and Antioxidant Activity of Polysaccharides from *Cordyceps militaris* Solid Medium. *Molecules* **2024**, *29*, 4560. [CrossRef] [PubMed]
33. Zhao, B.; Wang, X.; Liu, H.; Lv, C.; Lu, J. Structural characterization and antioxidant activity of oligosaccharides from Panax ginseng C. A. Meyer. *Int. J. Biol. Macromol.* **2020**, *150*, 737–745. [CrossRef] [PubMed]
34. Netala, V.R.; Hou, T.; Devarapogu, R.; Bethu, M.S.; Zhang, Z.; Vijaya, T. Exploring the therapeutic potential of triterpenoid saponins from Gymnema sylvestre: Mechanistic insights into hepatoprotection, immunomodulation, anticancer activities, molecular docking, and pharmacokinetics. *Heliyon* **2024**, *10*, e40850. [CrossRef] [PubMed]
35. Fan, P.; Han, B.; Hu, H.; Wei, Q.; Zhang, X.; Meng, L.; Nie, J.; Tang, X.; Tian, X.; Zhang, L.; et al. Proteome of thymus and spleen reveals that 10-hydroxydec-2-enoic acid could enhance immunity in mice. *Expert. Opin. Ther. Targets* **2020**, *24*, 267–279. [CrossRef] [PubMed]
36. Parente, I.A.; Chiara, L.; Bertoni, S. Exploring the potential of human intestinal organoids: Applications, challenges, and future directions. *Life Sci.* **2024**, *352*, 122875. [CrossRef] [PubMed]
37. Li, W.; Zhou, X.; Xu, S.; Cao, N.; Li, B.; Chen, W.; Yang, B.; Yuan, M.; Xu, D. Lipopolysaccharide-induced splenic ferroptosis in goslings was alleviated by polysaccharide of atractylodes macrocephala koidz associated with proinflammatory factors. *Poult. Sci.* **2022**, *101*, 101725. [CrossRef] [PubMed]
38. Dahiya, D.S.; Kichloo, A.; Tuma, F.; Albosta, M.; Wani, F. Radiation Proctitis and Management Strategies. *Clin. Endosc.* **2022**, *55*, 22–32. [CrossRef] [PubMed]
39. Suoa, K.; Zheng, C.; Li, Z.; Hao, L.; Zhu, J.; Zhao, C.; Shi, Y.; Yi, J.; Lu, J. Radioprotective effects of polysaccharides from Poria cocos peels against 60Co-γ induced oxidative damage in vitro and in vivo. *J. Future Foods* **2025**, *5–6*, 582–590. [CrossRef]
40. Thakkar, H.; Gangakhedkar, S.; Shah, R.P. Bioanalysis of Stress Biomarkers through Sensitive HILIC-MS/MS Method: A Stride toward Accurate Quantification of MDA, ACR, and CTA. *J. Am. Soc. Mass. Spectrom.* **2024**, *35*, 1110–1119. [CrossRef] [PubMed]
41. Vlašić, I.; Krstačić-Galić, A.; Horvat, A.; Oršolić, N.; Sadžak, A.; Mandić, L.; Šegota, S.; Jazvinšćak Jembrek, M. Neurotoxic Effect of Myricitrin in Copper-Induced Oxidative Stress Is Mediated by Increased Intracellular Ca^{2+} Levels and ROS/p53/p38 Axis. *Antioxidants* **2025**, *14*, 46. [CrossRef] [PubMed]
42. Zhao, J.; Wang, X.; Wang, Y.; Lv, G.; Lin, H.; Lin, Z. UPLC-MS/MS profiling, antioxidant and anti-inflammatory activities, and potential health benefits prediction of phenolic compounds in hazel leaf. *Front. Nutr.* **2023**, *10*, 1092071. [CrossRef] [PubMed]
43. Sharapov, M.G.; Gudkov, S.V.; Lankin, V.Z.; Novoselov, V.I. Role of Glutathione Peroxidases and Peroxiredoxins in Free Radical-Induced Pathologies. *Biochemistry* **2021**, *86*, 1418–1433. [CrossRef] [PubMed]
44. Peng, H.; Zhu, M.; Kong, W.; Tang, C.; Du, J.; Huang, Y.; Jin, H. L-cystathionine protects against oxidative stress and DNA damage induced by oxidized low-density lipoprotein in THP-1-derived macrophages. *Front. Pharmacol.* **2023**, *14*, 1161542. [CrossRef] [PubMed]
45. Li, C.; Meng, M.; Guo, M.; Wang, M.; Ju, A.; Wang, C. The polysaccharides from *Grifola frondosa* attenuate CCl4-induced hepatic fibrosis in rats via the TGF-β/Smad signaling pathway. *RSC Adv.* **2019**, *9*, 33684–33692. [CrossRef] [PubMed]
46. Mladenova, V.; Mladenov, E.; Stuschke, M.; Iliakis, G. DNA Damage Clustering after Ionizing Radiation and Consequences in the Processing of Chromatin Breaks. *Molecules* **2022**, *27*, 1540. [CrossRef] [PubMed]
47. Liu, Y.; Li, H.; Liu, W.; Guo, J.; Yang, H.; Tang, H.; Tian, M.; Nie, H.; Zhang, X.; Long, W. Design of Monovalent Cerium-Based Metal Organic Frameworks as Bioinspired Superoxide Dismutase Mimics for Ionizing Radiation Protection. *ACS Appl. Mater. Interfaces* **2022**, *14*, 54587–54597. [CrossRef] [PubMed]
48. Zhang, S.; Ao, P.; Chen, S.; Liao, X.; Chen, M.; Ruan, L.; Wei, L. Laminaria japonica Polysaccharide Alleviates Radiation-Induced Salivary Gland Injury by Promoting DNA Damage Repair. *Int. Dent. J.* **2026**, *76*, 109312. [CrossRef] [PubMed]

49. Goyal, R.K.; McManus, J.L.; Gopalakrishnan, M. Characterization of the Sequence of Cytopenia after Total-body Irradiation using Unsupervised Machine Learning. *Radiat. Res.* **2026**, *Epub ahead of printing*. [CrossRef] [PubMed]
50. Itoh, K.; Matsueda, S. Exploring the Potential of Humoral Immune Response to Commensal Bifidobacterium as a Biomarker for Human Health, including Both Malignant and Non-Malignant Diseases: A Perspective on Detection Strategies and Future Directions. *Biomedicines* **2024**, *12*, 803. [CrossRef] [PubMed]
51. Ran, Y.; Shen, X.; Li, Y. Glycyrrhiza Extract and Curcumin Alleviates the Toxicity of Cadmium via Improving the Antioxidant and Immune Functions of Black Goats. *Toxics* **2024**, *12*, 284. [CrossRef] [PubMed]
52. Wei, S.; Peng, W.; Zhang, C.; Su, L.; Zhang, Z.; Wang, J.; Huang, C.; Chu, Z. Cordyceps sinensis aqueous extract regulates the adaptive immunity of mice subjected to (60) Co γ irradiation. *Phytother. Res.* **2021**, *35*, 5163–5177. [CrossRef] [PubMed]
53. Wu, J.; Chen, G.; Chen, D.; Zhang, H.; Lv, H.; Wen, Z. *Grifola frondosa* Polysaccharides Alleviated Cyclophosphamide—Induced Intestinal Injury Based on Microbiota, Metabolite and Immune Axis Modulation. *Foods* **2025**, *14*, 3376. [CrossRef] [PubMed]
54. Lee, B.-H.; Pan, I.H.; Li, K.-C.; Cho, S.-C.; Huang, C.-H.; Hsu, W.-H. Probiotic mixture enhances spatial memory via gut-brain axis modulation in mice. *J. Funct. Foods* **2026**, *138*, 107211. [CrossRef]
55. Qiao, Z.; Li, Z.; Shi, Y.; Yi, J.; Zhu, J.; Kang, Q.; Hao, L.; Zhao, C.; Lu, J. Radiation protection of sodium alginate and its regulatory effect on intestinal microflora in mice. *Int. J. Biol. Macromol.* **2024**, *280*, 135809. [CrossRef] [PubMed]
56. Wang, M.; Dong, Y.; Wu, J.; Li, H.; Zhang, Y.; Fan, S.; Li, D. Baicalein ameliorates ionizing radiation-induced injuries by rebalancing gut microbiota and inhibiting apoptosis. *Life Sci.* **2020**, *261*, 118463. [CrossRef] [PubMed]
57. Hu, S.; Wang, J.; Xu, Y.; Yang, H.; Wang, J.; Xue, C.; Yan, X.; Su, L. Anti-inflammation effects of fucosylated chondroitin sulphate from Acaudina molpadioides by altering gut microbiota in obese mice. *Food Funct.* **2019**, *10*, 1736–1746. [CrossRef] [PubMed]
58. He, X.Y.; Zhu, Y.X.; Jiang, X.Q.; Zhu, F.R.; Luo, Y.J.; Qiu, Y.Y.; Huang, Z.A.-O.X.; Liu, B.A.-O.; Zeng, F. Probiotics-Fermented *Grifola frondosa* Total Active Components: Better Antioxidation and Microflora Regulation for Alleviating Alcoholic Liver Damage in Mice. *Int. J. Mol. Sci.* **2023**, *24*, 1406. [CrossRef] [PubMed]
59. Tu, J.; Kang, M.; Zhao, Q.; Xue, C.; Bi, C.; Dong, N. Oleanolic acid improves antioxidant capacity and the abundance of Faecalibacterium prausnitzii in the intestine of broilers. *Poult. Sci.* **2024**, *103*, 104340. [CrossRef] [PubMed]

Disclaimer/Publisher's Note: The statements, opinions and data contained in all publications are solely those of the individual author(s) and contributor(s) and not of MDPI and/or the editor(s). MDPI and/or the editor(s) disclaim responsibility for any injury to people or property resulting from any ideas, methods, instructions or products referred to in the content.